

Article

# Design of an Electromagnetic Variable Valve Train with a Magnetorheological Buffer

He Guo, Liang Liu \*, Xiangbin Zhu, Siqin Chang and Zhaoping Xu

School of Mechanical Engineering, Nanjing University of Science and Technology, Nanjing 210094, China; guoheyuyu@njjust.edu.cn (H.G.); 117101021486@njjust.edu.cn (X.Z.); changsq@njjust.edu.cn (S.C.); xuzhaoping@njjust.edu.cn (Z.X.)

\* Correspondence: l.liu@njjust.edu.cn; Tel.: +86-25-8430-3903

Received: 10 August 2019; Accepted: 17 October 2019; Published: 21 October 2019



**Abstract:** In this paper, an electromagnetic variable valve train with a magnetorheological buffer (EMVT with MR buffer) is proposed. This system is mainly composed of an electromagnetic linear actuator (EMLA) and a magnetorheological buffer (MR buffer). The valves of an internal combustion engine are driven by the EMLA directly to open and close, which can adjust the valve lift and phase angle of the engine. At the same time, MR buffer can reduce the seat velocity of the valve and realize the seat buffer of the electromagnetic variable valve. In this paper, the overall design scheme of the system is proposed and the structure design, finite element simulation of the EMLA, and the MR buffer are carried out. The electromagnetic force characteristics of the EMLA and buffer force of the MR buffer are measured, and the seat buffering performance is verified as well. Experiments and simulation results show that the electromagnetic force of the EMLA can reach 320.3 N when the maximum coil current is 40 A. When the current of the buffer coil is 2.5 A and the piston's motion frequency is 5 Hz, the buffering force can reach 35 N. At the same time, a soft landing can be realized when the valve is seated.

**Keywords:** camless; electromagnetic variable valve train; magnetorheological buffer; soft landing

## 1. Introduction

With global environmental issues being increasingly serious, the development of internal combustion engines is mainly focused on hybrid electric vehicles, electric vehicles, and alternative fuel vehicles. Hybrid electric vehicles combine a traditional internal combustion engine with a motor and hydraulic pump, which reduces harmful emissions of the internal combustion engine and effectively improves fuel economy. As one of the main components of hybrid electric vehicles, internal combustion engines still have an irreplaceable position [1–4]. Thus, the internal combustion engine will still comprise a large proportion of vehicles in the future.

As a variable valve mechanism, an electromagnetic variable valve train (EMVT) replaces the cam-driven valve mechanism in traditional engines and connects directly with the valve. Therefore, the limitation of the cam profile on valve timing is eliminated and the EMVT can adjust the valve lift and phase angle in real-time according to the engine operating conditions. The EMVT can also moderately increase the intake flow rate. Thus, the loss of pump gas and the power consumption of the valve train are reduced, and the fuel economy of the engine is improved. Xu et al. [5] have studied the influence of the EMVT on intake charge. The results show that the EMVT can improve the intake charging of the engine significantly. Fan et al. [6] realized the high compression ratio of the engine through EMVT. The results show that the thermal efficiency of the engine has an obvious improvement. Xinyu et al. [7] realized the optimization of exhaust valve motion by EMVT. The results show that the optimal exhaust valve opening motion can strengthen both the power performance and

fuel economy at engine part loads. However, since the linear actuator is connected with the valve directly, the mechanical damping coefficient of EMVT is low. Thus, the control performance of the EMVT is easily affected by the external disturbances coming from the cylinder gas force, friction force, and spring force, etc. Thus, excessive valve seating velocity may be produced in practical application, and excessive valve seat velocity will not only cause valve seat rebound and vibration noise, but also cause damage of engine components. The life and control accuracy of the internal combustion engine will be affected as well.

The seat buffer for the variable valve can be realized by adding a buffer structure or applying a valve control strategy. Due to the low damping coefficient of the EMVT, it is easily disturbed by external disturbances in practical application. Thus, adding a buffer structure to reduce the valve seat velocity is an effective solution. In the study of electro-hydraulic variable valve systems, Li et al. [8] realized the soft landing of the valve through a “buffer” composed of a hydraulic valve, plunger, and plunger sleeve; Yang et al. [9] and Chen et al. [10] designed a cushion structure to reduce the force of the valve seating, and the valve was buffered by the principle of a variable throttle area; Tu et al. [11] adopted a one-way throttle valve for buffering, and a genetic algorithm is adopted to optimize the control parameters of the throttle valve. In the research of electromagnetic variable valves, MIT [12] added a mechanical buffer between the electromagnetic linear actuator and the valve to reduce the valve velocity and system energy consumption. A seat cushion can be realized by designing the valve seat trajectory rationally [13–15]. In order to design the landing trajectory of the valve reasonably, it is necessary to control the valve to follow the trajectory in the process of movement. A seat cushion can also be realized by the control the valve seat velocity. The valve velocity is taken as the control target [16–20], and a closed-loop control strategy is carried out.

In this paper, an EMVT with an MR buffer is proposed, which consists of an electromagnetic linear actuator (EMLA) and a magnetorheological buffer (MR buffer). The EMLA is a moving coil linear actuator [21]. The EMLA generates a linear driving force through an electrified coil in the permanent magnet field. The driving force is positively correlated with the current intensity in the coil, and the engine valves are driven by the driving force. The MR buffer is mainly used to reduce the velocity of the valve before seating. The buffer force can be adjusted by changing the coil current intensity of the MR buffer to meet different valve seating velocity requirements. Thus, the damping characteristic of the system is adjusted by the MR buffer as well. The main feature of the system is that a buffer is set between the EMLA and the valve, which can change the cushioning force according to the valve seat velocity, and the damping coefficient of the system is adjusted in real-time by the MR buffer in actual operation. Thus, the system stability is improved while the valve seat velocity is reduced, and the soft landing of the valve is realized. At the same time, the valve lift and phase angle can be adjusted by the EMLA as well.

According to the above description, the valve opening lift and phase angle of an internal combustion engine can be adjusted by using EMVT instead of the traditional cam mechanism. Therefore, the valve state can be changed in real time according to the operating conditions of the internal combustion engine, so that the internal combustion engine can achieve the best power output and fuel consumption under all operating conditions. This is obvious for the preservation of internal combustion energy.

## 2. System Overview

In order to replace the traditional cam mechanism and complete the engine ventilation process successfully, the EMVT with the MR buffer needs to meet the following requirements:

1. It has a large mechanical damping coefficient, which can overcome the influence of external interference and parameter changes.
2. The valve seating velocity is controlled within 0.1 m/s. The EMLA and MR buffer is controlled by the control unit, and the seat velocity of the valve is reduced by the MR buffer to ensure the valve seat velocity is effectively controlled.

Figure 1 shows the structure of the EMVT with the MR buffer. As can be seen from Figure 1, the system consists of three main parts: the EMLA, MR buffer, and valve components. The structure of the EMLA mainly includes the inner and outer magnetic yokes, permanent magnets, coil frame, and electromagnetic coil. The electromagnetic coil is wound on the coil frame in series, and the electromagnetic coil is in a magnetic field generated by the permanent magnets. The axial motion law of the EMLA is controlled by changing the current intensity applied on the electromagnetic coil, thereby the valve is controlled. Compared with the conventional linear actuator, this EMLA cannot only realize the adjustable valve phase angle, but also realize the adjustable valve lift and transition time. The main function of the MR buffer is to reduce the seat velocity and restrain the rebound of the valve. The MR buffer mainly consists of a piston, piston rod, buffer coil, cylinder, end cover, and MR fluid. A groove is dug into the piston to wrap the buffer coil, and MR fluid flows through the annular gap between the piston and the cylinder to generate the buffer force. After the piston coil is energized, the magnetic force lines are mainly concentrated at the piston. Then, magnetic force lines enter the cylinder through the annular gap, and return to the piston through the annular gap on the other side to form a closed loop. The area of the annular gap through which the magnetic field lines pass is called the active region of the MR buffer. The MR fluid near this region will produce the MR effect due to the passage of magnetic force lines and, thus, produce a certain shear yield strength, and the reciprocating motion of the piston drives the MR fluid flow through the annular gap to provide a controllable buffer force.

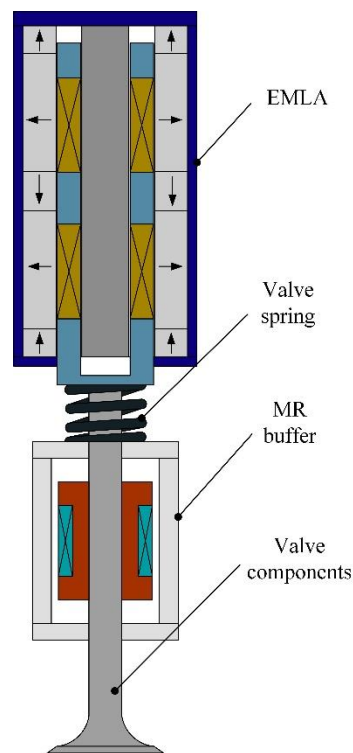


**Figure 1.** Structure of the EMVT with the MR buffer.

The EMLA and MR buffer are connected in series. A valve spring is installed between the EMLA and the MR buffer to provide a rebound force when the valve is closed. Thus, it can ensure the valve can be closed effectively.

The working principle of the EMVT with the MR buffer is described as follows: When the valve opens, the coil on the EMLA is energized. The coil is subjected to an axial electromagnetic force in the permanent magnetic field, which propels the valve to open. The opening time and lift of the valve controlled by the current intensity applied on the coil of the EMLA. When the EMLA drives the valve

to close, the buffer coil is energized before seating. The MR buffer generates a buffer force of a specified size and the force direction is opposite to the valve velocity. Thus, the seat velocity of the valve can be reduced and valve seat buffer can be realized.

Considering that the EMLA and MR buffer are two complex multi-physical field coupling systems, the independent design of the two main components is considered in the system design. Then the design results are verified by experiment.

### 3. Structure Design

#### 3.1. Structure Design of the Electromagnetic Linear Actuator

As the main driving component of the EMVT with the MR buffer, the EMLA shall meet the following requirements when being designed:

1. When the engine operates under high load, the pressure difference between the cylinder and the exhaust port can reach up to 8 bar when the exhaust valve is opened in the exhaust stroke [22]. Therefore, the maximum electromagnetic force of the EMLA needs to be over 300 N to ensure that the valve can be opened effectively.
2. In order to meet the requirements of the engine at high speed, the valve transition time (from 5% of the valve lift to 95% of the time experienced) can reach 4 ms, or even faster.
3. The EMLA is installed on the cylinder head of the engine, so the diameter and height should be limited to 40 mm and 70 mm, respectively, and can achieve a maximum power output under the volume limitation.
4. The change of the mover position should have less influence on the electromagnetic force of the EMLA.

In the finite element analysis software, the magnetic field of the air gap and electromagnetic force characteristics of the EMLA can be simulated by the finite element method, so that the structure of the EMLA can be reasonably designed. Figure 2a shows the magnetic finite element model of the EMLA established in MAXWELL provided by Ansoft in Pennsylvania, USA. The model mainly includes the inner and outer yokes, electromagnetic coil, permanent magnets, and air gap, where the coil is at the initial position and moves downward with a working stroke of 8 mm. The arrow at the permanent magnet region in Figure 2a represents the magnetization direction of the permanent magnets. Figure 2b shows the distribution of magnetic force lines and magnetic induction intensity obtained by simulation. As can be seen from Figure 2b, the magnetic force lines near the area of the electromagnetic coil are densely distributed and more uniform. The total magnetic force lines are symmetrically distributed. The color of different regions represents different magnetic induction intensities, and the magnetic induction intensity is mainly distributed in the inner yoke.

In the structure of the EMLA, different parameters such as the size of permanent magnets, the width of the air gap and the size of the inner and outer yokes will affect the electromagnetic force. The mass of the moving parts will affect the maximum acceleration of the moving parts, thus affecting the transition time of the EMLA. Under the condition of limited external size, the larger size of permanent magnets, and the smaller size of the air gap, a larger electromagnetic force can be generated. Excessive size of the permanent magnets will result in magnetic saturation of the yokes, and too small a size of the air gap will affect the installation space of the coil. Therefore, there are structural contradictions in the design of the EMLA. Thus, under the limited volume condition, the actuator should achieve as much power as possible, that is, to maximize the power density of the EMLA. In the finite element analysis software, the parametric analysis function is used to optimize the maximum acceleration that the moving parts can achieve. In the range of 40 mm diameter and 70 mm height, the air gap size, yokes size, and permanent magnet size are taken as optimization variables, and Table 1 shows the optimization results of the EMLA.

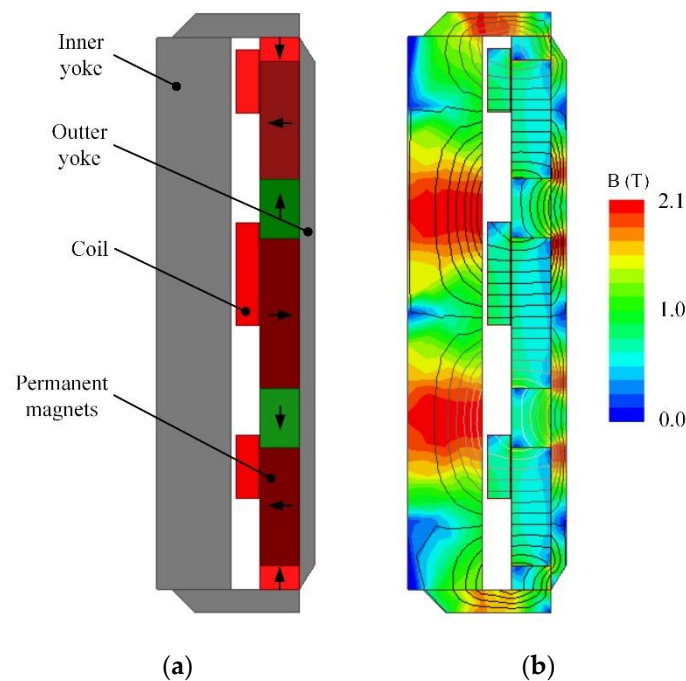


**Figure 2.** Magnetic field distribution of the EMLA: (a) Finite element model; (b) Magnetic field distribution.

**Table 1.** Main structure dimensions of the EMLA.

Parameter	Value
Stroke/mm	8
Diameter/mm	39
Height/mm	70
Volume/cm <sup>3</sup>	84
Permanent magnet thickness/mm	8
Mass of moving parts/g	114

As the coil frame moves up and down in the magnetic field formed by the permanent magnets, it is necessary to make non-conductive epoxy resin materials to prevent large eddy current losses in the coil frame. The magnetic field of the EMLA is mainly produced by the permanent magnets. Therefore, the quality of the permanent magnet material is related to the performance of the EMLA. NdFeB has high residual flux density, coercive, and magnetic energy products. Thus, it can be used as the permanent magnet material of the EMLA. The magnetic force lines of the permanent magnet in the EMLA needs to form a loop, and the loop needs to pass through the inner and outer yokes. Therefore, soft magnetic materials with high permeability are needed. In this paper, a low carbon steel material with similar properties to pure iron is selected as the material of the inner and outer yokes.

Figure 3 shows the electromagnetic force characteristic curve obtained by simulation. Electromagnetic force characteristics are described as the relationship between the electromagnetic force and the coil current intensity and coil position. The magnitude of the electromagnetic force varies with the current intensity and position of the coil. As can be seen from Figure 3, when the current intensity in the coil is 40 A, the maximum electromagnetic force that the EMLA can achieve is 320.3 N. At the same time, the EMLA has a certain end effect. When the position of the coil changes, the magnitude of the electromagnetic force fluctuates about 23 N, about 7% of the electromagnetic force. Therefore, the change of the mover position have less influence on the electromagnetic force, and the structure design requirements of the EMLA are realized [22].

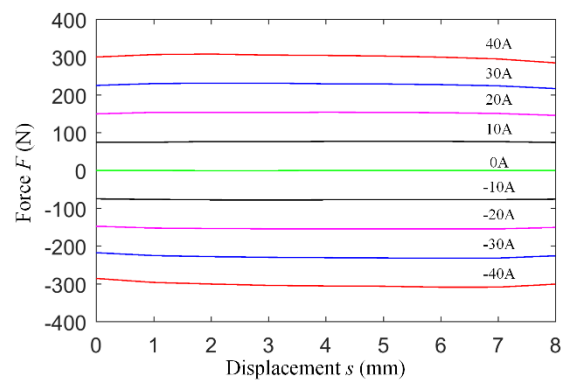


Figure 3. Electromagnetic force characteristic curve of the EMLA.

### 3.2. Structure Design of MR Buffer

The buffer force applied by the MR buffer mainly depends on the seat velocity of the valve and mass of the moving parts. Assuming a 5% displacement before valve closure as the seat buffer region, it is 0.4 mm before the valve seat, and according to the experimental data of the EMLA, the average seat velocity at this position is 0.5 m/s.

According to the law of dynamics, it can be obtained that:

$$F \times x = \frac{1}{2} m (v_1^2 - v_2^2) \quad (1)$$

where  $F$  is the buffering force when the valve is seated,  $x$  is the position when the valve is seated,  $m$  is the mass of the moving parts,  $v_1$  is the velocity before the valve is seated, and  $v_2$  is the velocity at the end of the valve. The total mass of the EMLA mover and valve components is 114 g. It is also assumed that the valve velocity at the end of the valve seating is 0 m/s. According to Equation (1), the required valve seat buffer force is 36.5 N. This data is calculated on the premise that 5% displacement before valve closure is used as seat buffer region. At this time, the EMLA drives the valve seat.

Figure 4 illustrates the structure and key parameters of the MR buffer. The main structure parameters affecting the buffer force include the piston diameter  $D$ , piston rod diameter  $d$ , piston effective length  $L$ , annular gap width  $h$ , and the performance parameters of the MR fluid, where the annular gap width  $h$  is the gap width between piston and cylinder, and the effective length  $L$  is the length of the other area on the buffer piston except the winding part. The structure design of the MR buffer is mainly based on the parameters mentioned above [23].

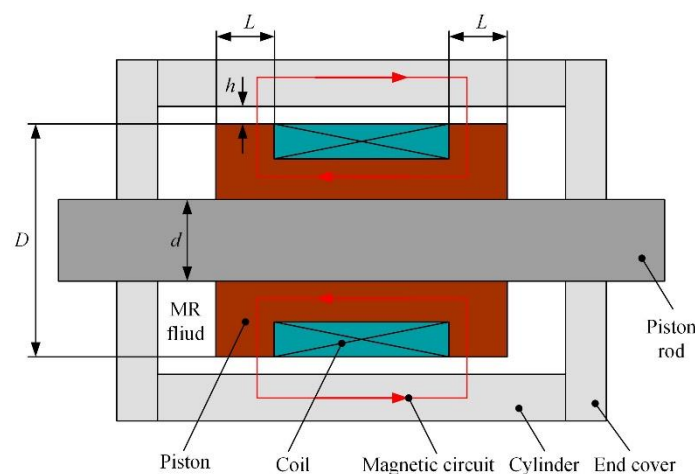


Figure 4. Structure of the MR buffer.

Considering the limited installation space of the buffer, the external size of the buffer should not be too large, and the diameter of the piston should be 20 mm. The piston rod is designed as a hollow rod so that the coil lead on the piston can be drawn from it. Therefore, the diameter of the piston rod should ensure that there is enough lead space. At the same time, the piston rod diameter should not be too large, otherwise it will affect the buffer force. Considering the above two factors, the diameter of the piston rod is 8 mm. The MR fluid was provided by Chongqing Materials Research Institute in Chongqing city, China. The magnetization curve is shown in Figure 5. Since the zero-field viscosity of the selected MR fluid is large (0.8 Pa\*s), it is necessary to select a larger annular gap width to achieve a smaller zero-field buffer force. However, too large an annular gap width will have an impact on the buffer force. Therefore, considering the above two factors, the annular gap width is 2.5 mm. The effective length of the piston is one of the main factors affecting the buffer force. Excessive effective length will result in a large appearance size of the MR buffer. Too small an effective length will lead to unstable output of buffer force. Therefore, considering the above two factors, the effective length is 10 mm. The main structural parameters of the MR buffer are shown in Table 2.

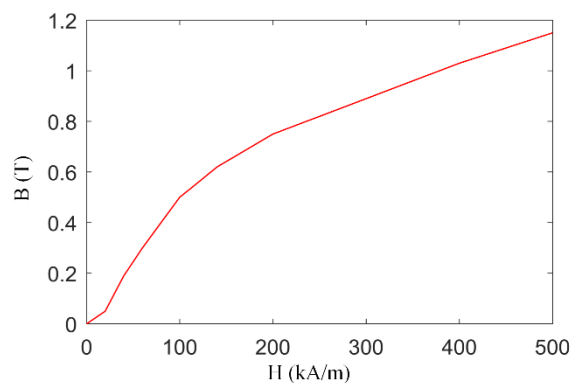


Figure 5. Magnetization characteristic curve of the MR fluid.

Table 2. Main structure dimensions of the MR buffer.

Parameter	Value
Cylinder inner diameter/mm	25
Piston diameter/mm	20
Piston rod diameter/mm	8
Effective length/mm	10
Annular gap width/mm	2.5
Cylinder outer diameter/mm	33
Stroke/mm	10

The finite element simulation of the magnetic field can be used to analyze the magnetic circuit of the MR buffer. Figure 6 shows the magnetic induction intensity and magnetic force line distribution of the MR buffer. Due to the axisymmetric structure of the MR buffer, only 1/2 of the finite element model of the MR buffer is established in the electromagnetic field simulation. As can be seen from Figure 6, the magnetic induction intensity at the annular gap is mainly concentrated near the effective length. The distribution of the magnetic induction intensity is uniform, and most of the magnetic force lines pass through the annular gap vertically.

The distribution curves of magnetic induction intensity at the annular gap under different coil current intensities are shown in Figure 7. As can be seen from Figure 7, the effective length of the buffer is the area where the magnetic field is mainly concentrated. The distribution of magnetic induction intensity in this region is more uniform, and the magnetic induction intensity outside the effective length is lower. With the increase of current intensity, the magnetic induction intensity at the effective length of the annular gap will also increase.

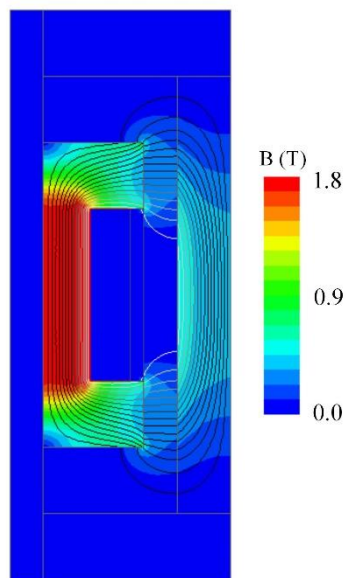


Figure 6. Magnetic field distribution of the MR buffer.

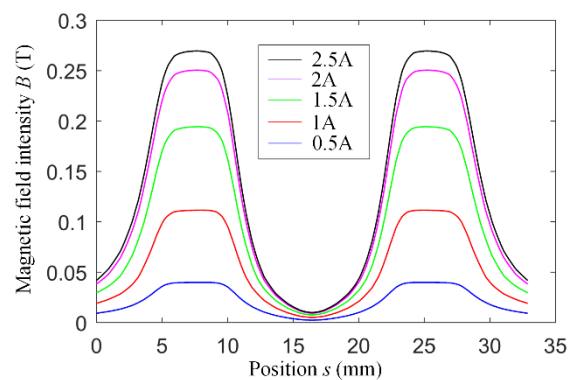


Figure 7. Magnetic induction intensity distribution curve in the annular gap.

#### 4. Multi-Physics FE Modeling and Simulation of the MR Buffer

Figure 8 shows the multi-physical field model of the MR buffer established in COMSOL Multiphysics provided by COMSOL in Stockholm, Sweden. The model involves the coupling of the magnetic field and flow field. The moving grid module drives the piston up and down in the model to simulate the buffer force.

The Navier–Stokes equation is used in the fluid region and the Maxwell equation is used in the magnetic field region. The coupling relationship between magnetic field and flow field can be achieved by two variables, hydrodynamic viscosity  $\eta$  and magnetic inductance intensity  $B$ . The coupling mode is shown in Table 3. The multi-physical field simulation model takes the simulation results of the magnetic field as one of the input values of the flow field [24].

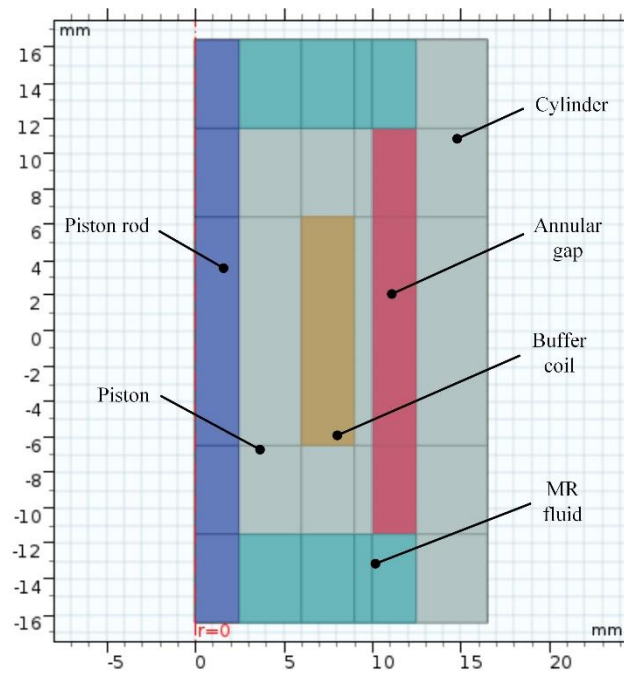


Figure 8. Multi-physical field model of the MR buffer.

Table 3. Multi-physical field equations.

Electromagnetic Equations (Maxwell)	Fluid Dynamics Equations (Navier–Stokes)
$\nabla \mathbf{E} = \frac{\rho_c}{\epsilon_0}$ <p>(Gauss Law)</p> $\nabla \mathbf{B} = 0$ <p>(Gauss Law for magnetism)</p> $\nabla \mathbf{E} = -\frac{\partial \mathbf{B}}{\partial t}$ <p>(Faraday Induction Law)</p> $\nabla \times \mathbf{B} = \mu_0 \mathbf{J} + \mu_0 \epsilon_0 \frac{\partial \mathbf{E}}{\partial t}$ <p>(Ampere Circuital Law)</p>	$\frac{\partial \rho}{\partial t} + \nabla(\rho \mathbf{u})$ <p>(Continuity)</p> $\rho \frac{\partial \mathbf{u}}{\partial t} + \rho \mathbf{u} \cdot \nabla \mathbf{u} = -\nabla p \mathbf{I} + \nabla \left\{ \eta(\dot{\gamma}, \mathbf{H}(\mathbf{B})) \left( \nabla \mathbf{u} + (\nabla \mathbf{u})^T - \frac{2}{3} (\nabla \mathbf{u}) \mathbf{I} \right) \right\} + f_m$ <p>(Momentum theorem)</p> <p>Viscosity coupling      Force coupling</p> <p>Constitutive equation</p> <p>(Bingham-Plastic model)</p> $\eta(\dot{\gamma}, \mathbf{H}(\mathbf{B})) = \eta_0 + \frac{\tau_y(\mathbf{H}(\mathbf{B})) \tanh(\zeta \dot{\gamma})}{\sqrt{\epsilon^2 + \dot{\gamma}^2}}$ <p>Magnetic force</p> $f_m = \mu_0 \chi \nabla \mathbf{H}^2 / 2$
<p>where: <math>\mathbf{E}</math>: Electric field, V/m;  <math>\mathbf{B}</math>: Magnetic inductance density, T;  <math>\mathbf{H}</math>: Magnetic field strength, A/m;  <math>\mathbf{J}</math>: Current density, A/m<sup>2</sup>;  <math>\rho_c</math>: Volumetric charge density, C/m<sup>3</sup>;  <math>\epsilon_0</math>: Permittivity of free space = <math>8.85 \times 10^{-12}</math>, F/m,  <math>\mu_0</math>: permeability of free space = <math>4\pi \times 10^{-7}</math>, N/A<sup>2</sup>.</p>	<p>where: <math>\mathbf{u}</math>: Velocity field, m/s;  <math>\rho</math>: Fluid density, kg/m<sup>3</sup>;  <math>\dot{\gamma}</math>: Shear strain rate, 1/s;  <math>\eta</math>: Dynamic viscosity, Pa*s;  <math>P</math>: Fluid zone pressure, Pa;  <math>\tau_y</math>: Yield stress, Pa;  <math>\zeta</math>: The constant;  <math>\epsilon</math>: Zoom factor,  <math>\chi</math>: Volume susceptibility.</p>

When the magnetic field is applied to the buffer, the MR fluid is characterized by Bingham fluid characteristics. The fluid flow and velocity distribution of a typical Bingham fluid between two parallel plates are shown in Figure 9. The MR fluid can be divided into three regions along the radial direction. The yield flow regions are on both sides and the plug flow region is in the middle. In the upper and lower regions near the plate, the MR fluid is yielding flow. At this region, the shear stress of the MR fluid is greater than the yield stress, and the MR fluid is in the flow state. The shear stress of the MR fluid in the middle plug flow region is less than its yield stress, and the MR fluid is in a relatively static state. In Figure 9, the active region is defined as the other region except the piston winding part at the annular gap. This region is the most obvious region where the MR fluid has MR effects.  $L$  is the length of the region.  $u$  and  $v$  are the velocity of the MR fluid and piston, respectively.  $h_1$ ,  $h_2$ , and  $h$  are the height of yield flow region, the height of the plug flow region, and the width of the annular gap, respectively.

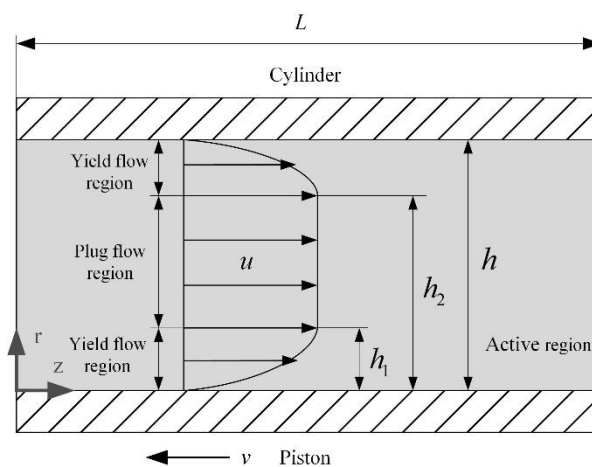


Figure 9. Fluid flow and velocity distribution of the MR fluid.

The Bingham model used to describe the properties of the MR fluid can be expressed as follows:

$$\begin{cases} \tau = \mu_0\gamma + \tau_y, & \tau > \tau_y \\ \gamma = 0, & \tau \leq \tau_y \end{cases} \quad (2)$$

where  $\mu_0$  is the zero field viscosity of the MR fluid,  $\tau$  is the actual yield strength of the MR fluid,  $\gamma$  is the shear rate of the MR fluid, and  $\tau_y$  is the ultimate yield strength of the MR fluid.

However, due to the non-differentiability of the plug flow region in the model, it will lead to complications in the actual calculation process. One way to solve this problem is to first determine the boundary of the plug flow regions, and then describe the region as a region with a constant velocity vector. This approach, however, assumes a fully developed flow and become very difficult when dealing with complex annular gap geometries. Thus, it does not have universal applicability.

The method used in this paper is the Bingham plastic model proposed by Case et al. [25]. In this model, the continuous differentiability of yield stress is achieved by describing the plug flow region as a micro-flow region.

This model is described as:

$$\tau = \left( \frac{\tau_y \tanh(\xi\gamma)}{\sqrt{\varepsilon^2 + \gamma^2}} + \mu_0 \right) \gamma \quad (3)$$

where  $\xi$ ,  $\varepsilon$  are constant coefficients.

By dividing the two sides of Equation (3) by the shear stress  $\gamma$  at the same time, the viscosity formula of the MR fluid can be obtained as follows:

$$\mu = \frac{\tau_y \tanh(\xi \gamma)}{\sqrt{\varepsilon^2 + \gamma^2}} + \mu_0 \quad (4)$$

In the multi-physical field simulation software, the correlation between the magnetic inductance intensity  $B$  and the fluid viscosity  $\mu$  at each node of the annular gap can be set up by Equation (4), so as to realize the multi-physical field coupling calculation of the magnetic field and the flow field.

In the simulation, the mesh is divided into moving meshes. The motion equation of the piston part is set to a sine with a frequency of 5 Hz and an amplitude of 4 mm. At the same time, the current in the buffer coil is set to 0 A, 1 A, and 2.5 A, respectively. Constant coefficients  $\xi$  and  $\varepsilon$  are set to 0.03 and 0.1, respectively. In the model, the integral of the total stress along the axis on the boundary of piston and piston rod is the result of the buffer force obtained by simulation.

Figures 10–12 show the velocity distribution and dynamic viscosity distribution of the MR fluid in the MR buffer. As can be seen from the figure, the dynamic viscosity of the MR fluid increases significantly in the active region of the MR buffer, and compared with other fluid regions, the flow velocity of the active region decreases significantly. The results show that the MR fluid in the active region have an MR effect and the dynamic viscosity increases due to the influence of the magnetic field.

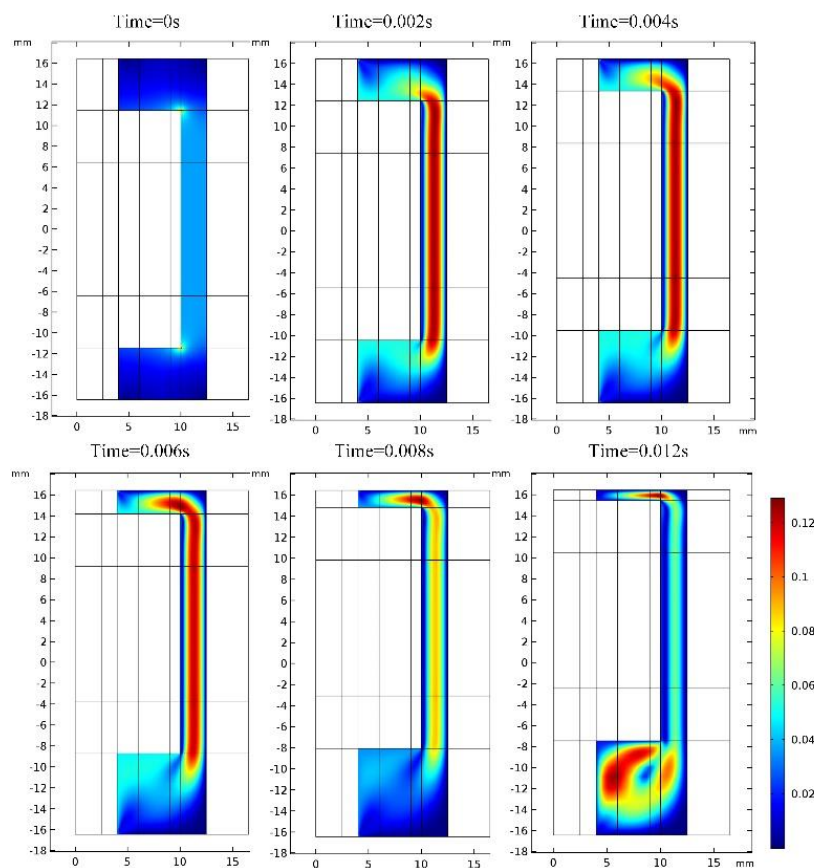


**Figure 10.** Velocity distribution map of the MR fluid when the current is 0 A.

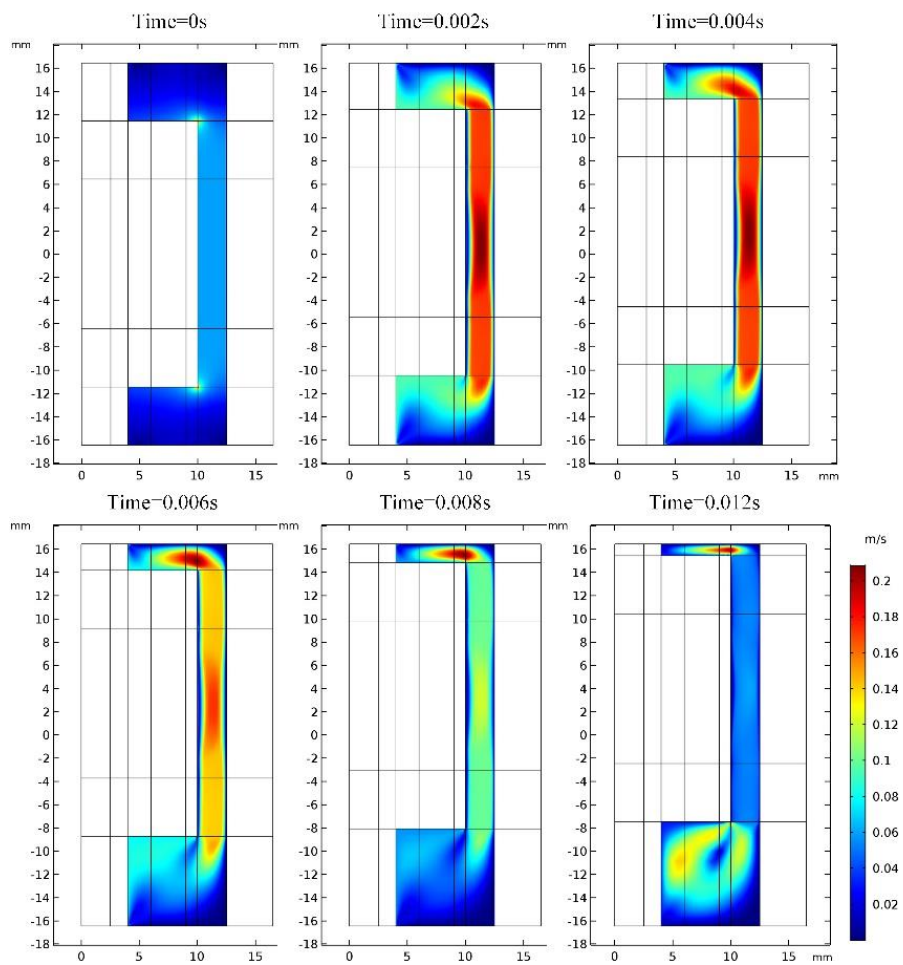


**Figure 11.** Velocity distribution map of the MR fluid when the current is 2.5 A.

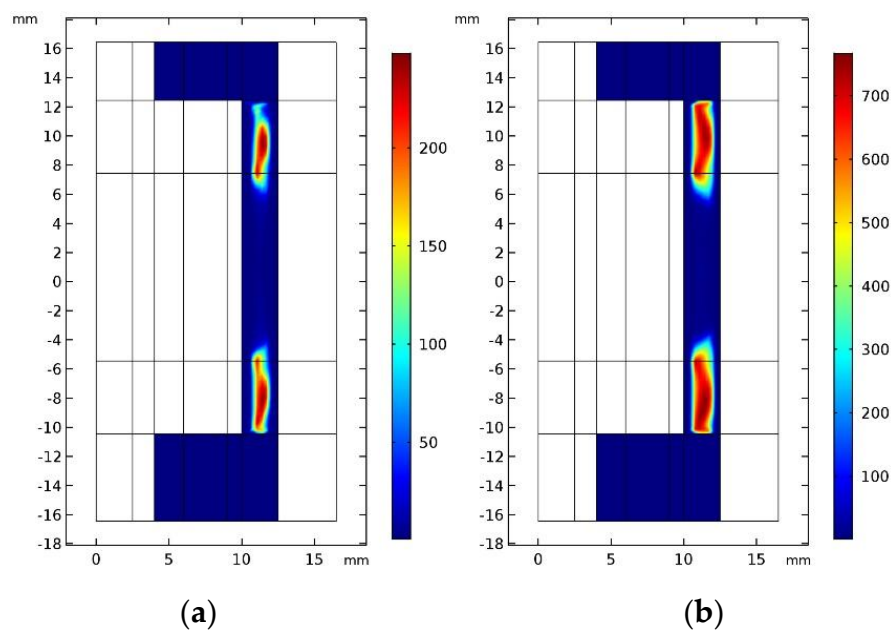


**Figure 12.** Dynamic viscosity distribution map of the MR fluid: (a)  $I = 1$  A; (b)  $I = 2.5$  A.

## 5. Validation with Experimental Results

### 5.1. Electromagnetic Force Characteristic Experiment of the EMLA

This experiment mainly measures the electromagnetic force characteristic curve of the EMLA, and compares with the simulation results to verify the accuracy of the simulation model. Figure 13 shows the experimental bench for measuring the electromagnetic force characteristic of the EMLA. The experimental bench includes the EMLA, displacement sensor (500LCIT series displacement sensors), force sensor (LSR type tension pressure sensor, with a maximum range of 200 N), adjusting screw rod, and baffle. The displacement sensor and the force sensor are used to measure the displacement and electromagnetic force of the mover, respectively. The measured data are fed back to the PC for data processing. The adjusting screw rod is mainly used to adjust the position of the mover. The position of the mover is changed by 1 mm for every turn of the screw. The EMLA is the control objective.

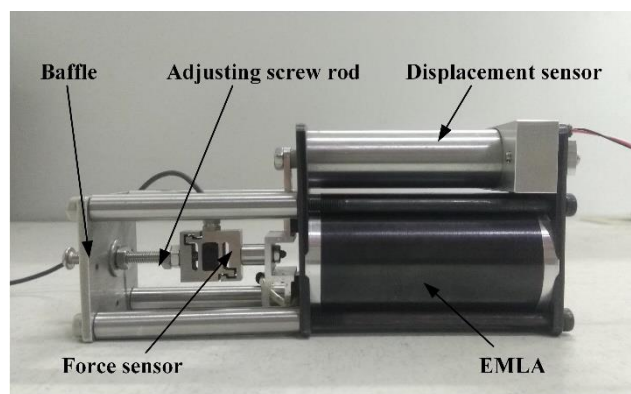


**Figure 13.** Experimental bench for the electromagnetic force characteristic.

In this experiment, the position of the mover is changed by adjusting the screw, and current intensities of 5 A, 10 A, and 15 A is applied to the electromagnetic coil to measure the electromagnetic force characteristic curve of the EMLA. Figure 14 shows a comparison between the measured electromagnetic force characteristic curve and the simulated curve. As can be seen from the figure, the electromagnetic force characteristic curves obtained from the experiment and simulation are in good agreement. The electromagnetic force is proportional to the current, and it changes very little with the change of the mover position. This shows that the magnitude of the electromagnetic force is only slightly affected by the change of the mover position, which meets the requirements of the structural design.

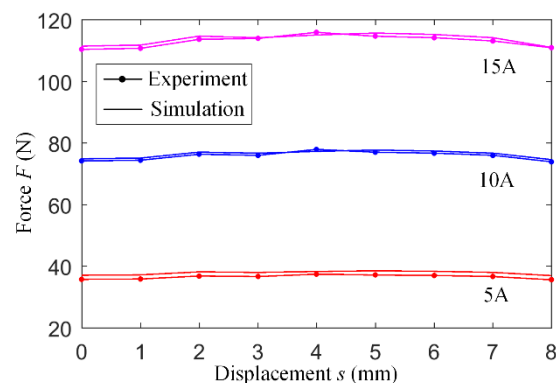


**Figure 14.** Electromagnetic force characteristic curve of the EMLA.

## 5.2. MR Buffer Force Measurement

This experiment mainly measures the buffer force of the MR buffer, where a constant current intensity is applied in the buffer coil, and the piston reciprocates in a sinusoidal curve. Then the experiment results and simulation results are compared and analyzed. An experimental bench for measurement is shown in Figure 15. The experimental bench includes the EMLA, displacement sensor, force sensor, and MR buffer. The displacement sensor and force sensor are used to collect the displacement data and buffer force data in the experiment and feed them back to the controller and PC for data processing. The EMLA and MR buffer are the control objectives. In the experiment, the EMLA drives the buffer piston to reciprocate at frequencies of 1 Hz, 3 Hz, and 5 Hz, respectively, and the sinusoidal wave amplitude is 4 mm. At the same time, currents of 1 A and 2.5 A are applied to the buffer coil, respectively.

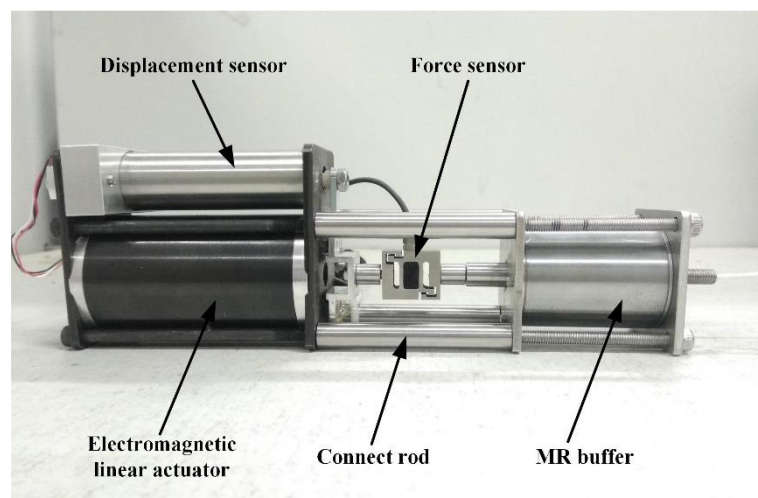


Figure 15. Experimental bench for the buffer force measurement.

Figure 16 shows a comparison between the experimental displacement–velocity curve and the target displacement–velocity curve of the MR buffer. As can be seen from Figure 16, a sudden change in the curve occurs during the start point and stroke end point. The reason for the sudden change is that the static friction will affect the displacement curve of the buffer piston at the beginning of the movement and reversal, which makes the experimental curve not follow the target curve.

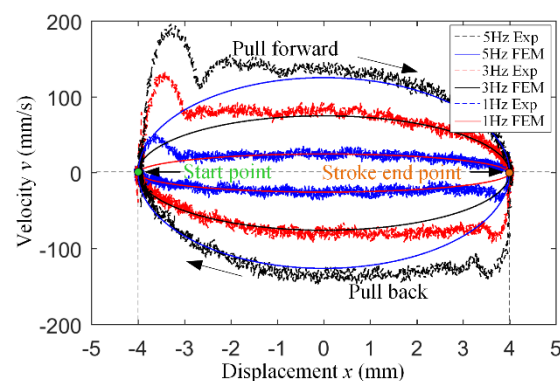
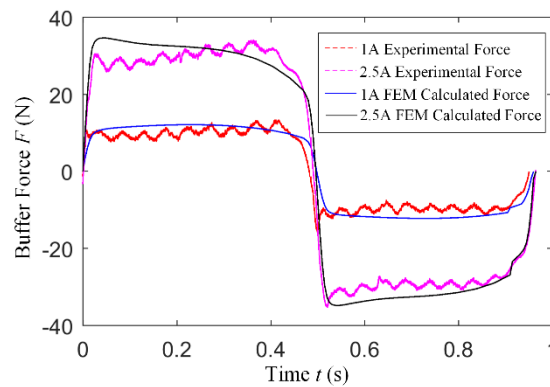


Figure 16. Displacement–velocity curve of the MR buffer.

Figures 17–19 show comparisons between the experimental buffer force curve and the simulation curve. As can be seen from the figures, when the piston motion frequency is 5 Hz and the buffer coil current is 1 A and 2.5 A, the maximum buffer force measured is 10 N and 35 N, respectively. At the

same time, the buffer force measured by different coil current intensities is different, showing that the coil current intensity is the main factor affecting the buffer force. As can be seen from the figures, the simulation results are in good agreement with the experimental results. The main deviation occurs at the piston's starting and reversing position. Due to the sudden change of displacement at this location, the measured buffer force curve will produce a certain sudden change at this location, and the mutation becomes more obvious as the frequency increases.



**Figure 17.** Buffer force curve at 1 Hz frequency.

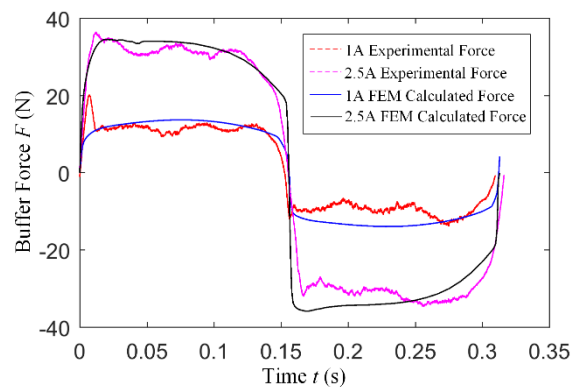


**Figure 18.** Buffer force curve at 3 Hz frequency.

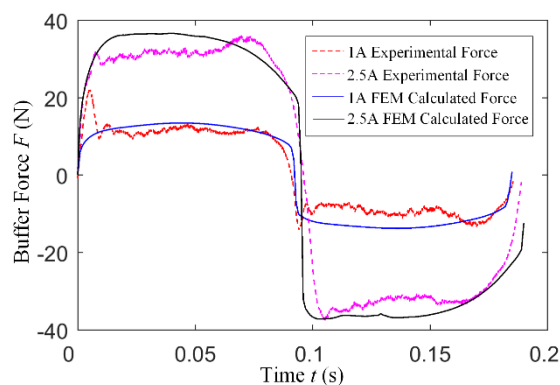


**Figure 19.** Buffer force curve at 5 Hz frequency.

### 5.3. Seating Performance Experiment

The main purpose of this experiment is to verify the seat buffering effect of the EMVT with the MR buffer. The experimental bench is shown in Figure 20. The experimental bench includes the EMVT with the MR buffer, displacement sensor, and valve components. Where the EMVT with the MR buffer is the control object, a displacement sensor is used to measure the displacement curve of the mover.

In this experiment, the EMLA is used to drive the valve opening and closing. The buffer effect of the system is verified by applying the buffering force before the valve seating.

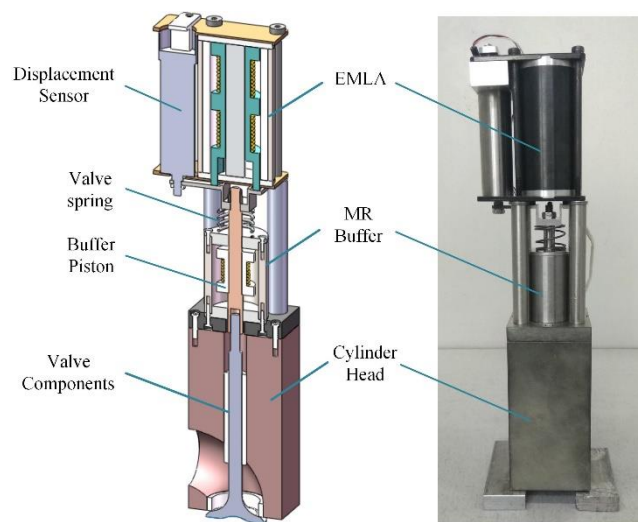


Figure 20. Valve seating test bench.

Figure 21 shows the experimental curve of the valve seat velocity and displacement when the valve lift is 8 mm. In this experiment, the coil in the buffer is energized before the valve seat to generate the buffering force, so as to reduce the valve seat velocity and realize the valve seat buffering. As can be seen from Figure 21, when the valve lift is 8 mm, the valve seat velocity decreases from 0.58 m/s to 0.14 m/s, and the valve rebound height decreases from 0.2 mm to 0.05 mm. The result shows that by applying buffering force before valve seat can reduce the valve seat velocity and restrain the valve rebound effectively. The seat buffer performance of the system is good.

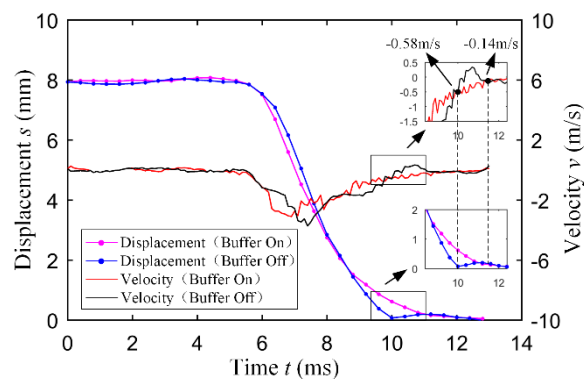


Figure 21. Experimental result of seating performance when the valve lift is 8 mm.

## 6. Conclusions

In this paper, an EMVT with an MR buffer is designed. The structure scheme of the system is put forward and the main components of the EMLA and MR buffer are designed. According to the structure of the main components, the magnetic field simulation of the EMLA and the MR buffer and the multi-physical field simulation of the MR buffer are carried out, respectively, allowing an accurate estimation of the magnetic force and buffer force. Electromagnetic simulation results show that the maximum electromagnetic force that EMLA can achieve is 320.3 N. The experimental bench of the system is built, and the measured buffer can achieve a 35 N buffer force when the piston motion frequency is 5 Hz and the buffer coil current is 2.5 A. The experimental results are in good agreement with the simulation results. The seating performance of the system is verified. When the lift of the

valve is 8 mm, the seating velocity of the valve decreases from 0.58 m/s to 0.14 m/s, and the rebound height of the valve decreases from 0.2 mm to 0.05 mm. From the above results, the system can meet the electromagnetic force required when the valve is opened and the buffer force required when the valve is buffered, and it can reduce the valve seat velocity and restrain the seat rebound effectively. Therefore, the system has good seat buffering performance.

The requirements of the EMLA and MR buffer are higher for the EMVT with MR buffer. It not only requires the EMLA to have a large electromagnetic force, but also ensures that the buffering force can achieve seat buffering and quick response. Therefore, the EMVT with the MR buffer still needs further research on the buffering force response time of the MR buffer and the structure optimization of the system.

**Author Contributions:** Supervision: L.L., S.C., and Z.X.; research—original draft—editing: H.G.; system control: X.Z.

**Funding:** This work was supported by the National Natural Science Foundation of China (Grant No. 51975297, 51875290) and Shanghai Aerospace Science and Technology Innovation Fund (SAST2018-107).

**Conflicts of Interest:** The authors declare no conflict of interest.

## References

1. Su, W.H.; Zhang, Z.J.; Liu, R.L. Development trend of automotive internal combustion engine technology. *China Eng. Sci.* **2018**, *20*, 97–103. [[CrossRef](#)]
2. Leone, T.; Pozar, M. Fuel economy benefit of cylinder deactivation—Sensitivity to vehicle application and operating constraints. *SAE Trans.* **2001**, *110*, 2039–2044. [[CrossRef](#)]
3. Millo, F.; Mirzaeian, M.; Luisi, S.; Doria, V.; Stroppiana, A. Engine displacement modularity for enhancing automotive s.i. engines efficiency at part load. *Fuel* **2016**, *180*, 645–652. [[CrossRef](#)]
4. Li, R.C.; Zhu, G.G. A real-time pressure wave model for knock prediction and control. *Int. J. Engine Res.* **2019**, 1–15. [[CrossRef](#)]
5. Xu, J.; Chang, S.; Fan, X.; Fan, A. Effects of electromagnetic intake valve train on gasoline engine intake charging. *Appl. Therm. Eng.* **2016**, *96*, 708–715. [[CrossRef](#)]
6. Fan, X.; Chang, S.; Liu, L.; Lu, J. Realization and optimization of high compression ratio engine with electromagnetic valve train. *Appl. Therm. Eng.* **2017**, *112*, 371–377. [[CrossRef](#)]
7. Fan, X.Y.; Chang, S.Q. Electromagnetic Exhaust Valve Event Optimization for Enhancing Gasoline Engine Performance. *MATEC Web Conf.* **2017**, *95*, 15009. [[CrossRef](#)]
8. Li, H. *Cam-Free Electro-Hydraulic Variable Valve Mechanism Control of Internal Combustion Engine Based on Model*; Beijing Institute of Technology: Beijing, China, 2018.
9. Yang, J.; Wang, Z.C.; Wang, Y. Design and analysis of electronically controlled hydraulic fully variable valve driving system. *J. Hunan Univ. Nat. Sci. Ed.* **2017**, 2017. [[CrossRef](#)]
10. Chen, F. Simulation and experimental research of hydraulic pressure and intake valve lift on a fully hydraulic variable valve system for a spark-ignition engine. *Adv. Mech. Eng.* **2018**, *10*, 1–11. [[CrossRef](#)]
11. Tu, B.; Tian, H.; Wei, H.Q. Research on buffering process of electro hydraulic drive variable gas mechanism. *China Mech. Eng.* **2016**, *27*, 2652–2658. [[CrossRef](#)]
12. Paden, B.A.; Snyder, S.T.; Paden, B.E. Modeling and Control of an Electromagnetic Variable Valve Actuation System. *IEEE/ASME Trans. Mechatron.* **2015**, *20*, 2654–2665. [[CrossRef](#)]
13. Reinholz, B.; Seethaler, R. Experimental Validation of a Cogging Torque Assisted Valve Actuation System for Internal Combustion Engines. *IEEE/ASME Trans. Mechatron.* **2016**, *21*, 453–459. [[CrossRef](#)]
14. Gillella, P.K.; Song, X.; Sun, Z. Time-Varying Internal Model-Based Control of a Camless Engine Valve Actuation System. *IEEE Trans. Control Syst. Technol.* **2014**, *22*, 1498–1510. [[CrossRef](#)]
15. Reinholz, B.A.; Reinholz, L.; Seethaler, R.J. Optimal trajectory operation of a cogging torque assisted motor driven valve actuator for internal combustion engines. *Mechatronics* **2018**, *51*, 1–7. [[CrossRef](#)]

16. Haus, B.; Aschemann, H.; Mercorelli, P.; Werner, N. Nonlinear modelling and sliding mode control of a piezo-hydraulic valve system. In Proceedings of the 2016 21st International Conference on Methods and Models in Automation and Robotics (MMAR), Miedzyzdroje, Poland, 29 August–1 September 2016; pp. 442–447. [[CrossRef](#)]
17. Samani, R.; Khodadadi, H. A particle swarm optimization approach for sliding mode control of electromechanical valve actuator in camless internal combustion engines. In Proceedings of the IEEE International Conference on Environment & Electrical Engineering & IEEE Industrial & Commercial Power Systems Europe, Milan, Italy, 6–9 June 2017. [[CrossRef](#)]
18. Di Gaeta, A.; Hoyos Velasco, C.I.; Montanaro, U. Cycle-by-Cycle Adaptive Force Compensation for the Soft-Landing Control of an Electro-Mechanical Engine Valve Actuator. *Asian J. Control* **2014**, *17*, 1707–1724. [[CrossRef](#)]
19. Bernard, L.; Ferrari, A.; Micelli, D.; Perotto, A.; Rinolfi, R.; Vattaneo, F. Electrohydraulic Valve Control with MultiAir Technology. *MTZ Worldwide* **2009**, *70*, 4–10. [[CrossRef](#)]
20. Yang, Y.P.; Liu, J.J.; Ye, D.H. Multi-objective Optimal Design and Soft Landing Control of an Electromagnetic Valve Actuator for a Camless Engine. *IEEE/ASME Trans. Mechatron.* **2013**, *18*, 963–972. [[CrossRef](#)]
21. Fan, X.; Chang, S.; Lu, J.; Liu, L.; Yao, S.; Xiao, M. Energy consumption investigation of electromagnetic valve train at gas pressure conditions. *Appl. Therm. Eng.* **2019**, *146*, 768–774. [[CrossRef](#)]
22. Zhang, L.L. *Research on Engine Valve Load Characteristics and Design of Simulation Loading System*; Nanjing University of Science and Technology: Nanjing, China, 2019.
23. Case, D.; Taheri, B.; Richer, E. Design and Characterization of a Small-Scale Magneto-rheological Damper for Tremor Suppression. *IEEE/ASME Trans. Mechatron.* **2013**, *18*, 96–103. [[CrossRef](#)]
24. Sternberg, A.; Zemp, R.; De La Llera, J.C. Multi-physics behavior of a magneto-rheological damper and experimental validation. *Eng. Struct.* **2014**, *69*, 194–205. [[CrossRef](#)]
25. Case, D.; Taheri, B.; Richer, E. Dynamical Modeling and Experimental Study of a Small-Scale Magnetorheological Damper. *IEEE/ASME Trans. Mechatron.* **2014**, *19*, 1015–1024. [[CrossRef](#)]



© 2019 by the authors. Licensee MDPI, Basel, Switzerland. This article is an open access article distributed under the terms and conditions of the Creative Commons Attribution (CC BY) license (<http://creativecommons.org/licenses/by/4.0/>).